Sandwichlike strain glass phase diagram of $Ti_{49}Ni_{51-x}Pd_x$

Shuai Ren,[1,*] Chao Zhou,[1] Dezhen Xue,[1,†] Dong Wang,[1] Jian Zhang,[1]
Xiangdong Ding,[1] Kazuhiro Otsuka,[2] and Xiaobing Ren[1,2,‡]
[1]*Frontier Institute of Science and Technology, and State Key Laboratory for Mechanical Behavior of Materials, Xi'an Jiaotong University, Xi'an 710049, China*
[2]*Ferroic Physics Group, National Institute for Materials Science, Tsukuba, 305-0047 Ibaraki, Japan*
(Received 13 June 2016; revised manuscript received 7 November 2016; published 23 December 2016)

Two kinds of phase diagrams can be observed in doped ferroic materials. A glass phase diagram is formed by doping a nontransforming end into a ferroic matrix, while doping a transforming end forms phase diagrams with a phase boundary separating two different ferroic phases. Here we report a phase diagram in which a strain glass state is sandwiched between two distinct ferroelastic phases. This type of phase diagram in doped ferroelastic materials bridges the one with a glass state and the one with a phase boundary. We thus establish a 3D phase diagram of $Ti_{50-y}Ni_{50+y-x}Pd_x$ ternary alloys, in which the evolution of these different kinds of phase diagrams can be observed. An understanding from the Landau free energy landscape suggests that the transforming doping end plays three roles in influencing the ferroic matrix: (1) to destabilize the ferroic matrix phase, (2) to stabilize another ferroic phase different from the matrix one, and (3) to create random local fields. The competition between these effects determines various phase diagrams in doped ferroic materials. Thus our work may provide an experimental foundation for a unified mechanism to all three kinds of phase diagrams.

DOI: 10.1103/PhysRevB.94.214112

I. INTRODUCTION

Doping with defects is a common approach to improve various physical properties of materials [1]. The well-known examples include acceptor/donor-doped Si, which forms the P-N junction, serving as the base of modern electronic industry [2]. Doping also plays a crucial role in ferroic materials, an important subgroup of smart materials which respond hysteretically to electric, mechanical, or magnetic fields [3]. For example, doping results in various interesting phenomena in ferroic materials, ranging from the glassy transition [4–11] to the morphotropic phase boundary [12–17] to the aging effect [18]. Those phenomena can either improve the functional properties significantly or give rise to new physics.

The quenched-in disorders or defects give rise to the frustration in a ferroic property (usually the ferroic order parameter) such as strain, polarization, or magnetization, and thus result in a glassy state in ferroic materials [19–21]. The glassy state possesses a frozen and frustrated local ordering of the ferroic order parameters rather than a long-range ferroic ordering [19–21]. It is manifest in its nonergodic response and slow dynamics [7,22]. Experimentally, the glassy phase is obtained by doping a nontransforming end (without spontaneous symmetry-breaking transformation) into a ferroic matrix (with spontaneous symmetry-breaking transformation) [4–11]. The nontransforming end can be considered as point defects which create random local fields to hinder the long-range ordering of ferroic order parameters [23–26]. With increasing concentration of the nontransforming end, the long-range ferroic ordering of the transforming matrix gradually loses its thermodynamic stability. After the concentration exceeds a critical value, the long-range ordering breaks whereas the short-range ordering persists. In the past decades, such a glassy state has been found in three primary ferroic systems (i.e., ferromagnetics, ferroelectrics, and ferroelastics), and examples include strain glass in $Ti_{50}(Ni_{50-x}D_x)$ (D=Fe, Co, Cr, Mn) ferroelastic alloys [27,28], relaxors in La-doped PZT ferroelectric ceramics [29,30], and cluster spin glass in Au-Fe binary alloys [31]. These reported glass-state-involved phase diagrams in three ferroic systems possess a similar configuration; i.e., there is a phase boundary separating a ferroic long-range phase and a glassy state.

Differently from the above glass phase diagram, the phase diagram constructed by two transforming ends (both with spontaneous symmetry-breaking transformation) generally possesses a phase boundary separating two different long-range-ordered ferroic phases [12–15]. The most well-known example is the phase diagram of lead zirconium titanate (PZT) in which a phase boundary separating tetragonal and rhombohedral ferroelectric phases allows giant piezoelectric responses [12,13]. This phase boundary was termed the morphotropic phase boundary (MPB), where the competition between the two long-range ferroic orderings makes the variation of order parameters fairly easy [12,15]. Recently, such an MPB phase diagram was also discovered in ferromagnetics where giant magnetostriction was obtained [16,17]. Moreover, similar phase diagrams with a phase boundary separating two different ferroelastic phases exist in $Ti_{50}Ni_{50}$-$Ti_{50}M_{50}$ (M=Pt, Au, Pd) shape memory alloys/ferroelastic systems as well [32–37]. All of the MPB phase diagrams are characterized by a phase boundary separating two different long-range-ordered ferroic phases.

Glass and MPB phase diagrams have been widely studied for decades, but in a separate manner. The linking between these two types of doping-induced phase diagrams is seldom concerned. It seems that the nontransforming doping end results in a glass phase diagram, while doping with the transforming end leads to an MPB phase diagram. In the present study, we showed that doping with the transforming

*francis.rens@gmail.com
†xuedezhen@mail.xjtu.edu.cn
‡ren.xiaobing@nims.go.jp

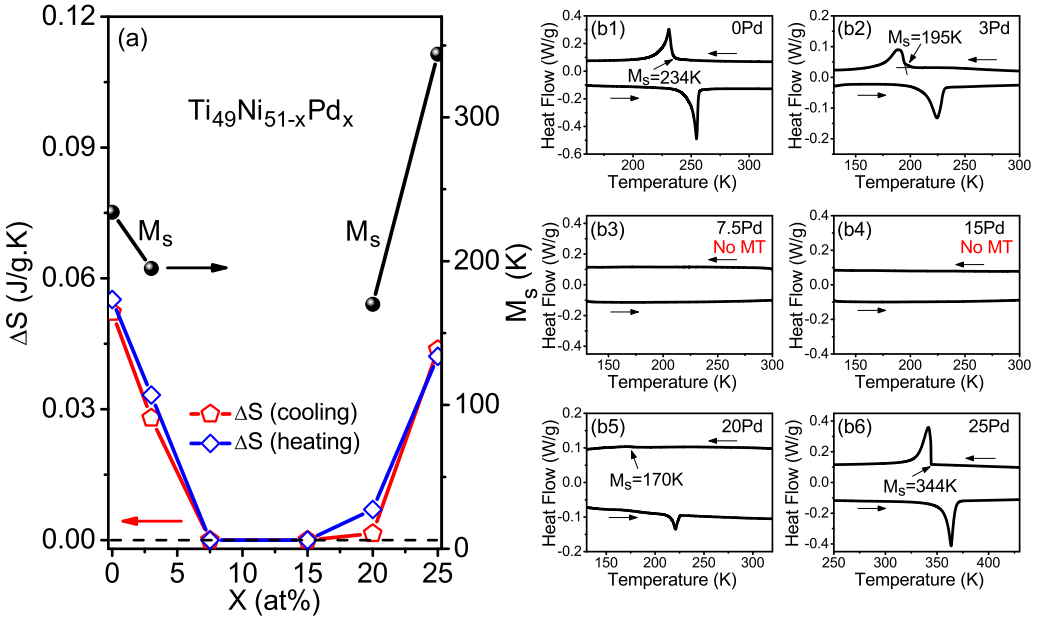

FIG. 1. (a) The martensitic transformation start temperature (M_s) and entropy change (ΔS) during martensitic and reverse martensitic phase transformations in $Ti_{49}Ni_{51-x}Pd_x$ alloys as a function of Pd concentration. (b1)–(b6) DSC curves of several typical compositions: (b1) 0Pd, (b2) 3Pd, (b3) 7.5Pd, (b4) 15Pd, (b5) 20Pd, and (b6) 25Pd.

end can give rise to a glassy state instead of MPB. Furthermore, a sandwichlike strain glass phase diagram in $Ti_{49}Ni_{51-x}Pd_x$ was established, where two different ferroelastic phases exist at two sides respectively and a strain glass state is sandwiched in between. In orientational glasses, phase diagrams with a similar shape where two long-range orientational orders are separated by a glassy state have been reported [38,39]. But how this kind of phase diagram relates with glass and MPB phase diagrams is still unclear. We then established a three-dimensional phase diagram, which bridges the glass and MPB, and it may be helpful to develop a unified understanding on all the doping-induced phase diagrams in ferroic materials.

II. EXPERIMENTAL PROCEDURE

Samples of $Ti_{49}Ni_{51-x}Pd_x$ alloys ($x = 0 \sim 25$, abbreviated by xPd hereafter) were prepared from highly pure metals (>99.95 at.%) by arc-melting under an argon atmosphere. The specimens were solution-treated at 1273 K for 24 h in evacuated quartz tubes, followed by water quenching. After hot rolling, the specimens were solution-treated at 1273 K for 1 h and subsequently quenched into water again. Latent heat of transformation was measured with a differential scanning calorimeter (DSC-Q200 from TA Company) with a cooling/heating rate of 10 K/min. Electrical resistivity (ER) of specimens was measured through a four-probe method with a constant current of 100 mA and a cooling/heating rate of 2K/min. *In situ* x-ray diffraction (Shimadzu 7000 XRD) measurement from high temperature to low temperature was used to identify the possible structural change. The possible strain glass transition was detected by dynamic mechanical analysis (DMA-Q800 from TA Instruments) using a step cooling method with a single cantilever mode in the frequency range from 0.2 to 20 Hz.

III. RESULTS

The composition dependence of entropy change (ΔS) in both cooling and heating processes [Fig. 1(a)] exhibits an unexpected U curve, which is calculated by $\Delta S = \Delta H/M_s$ (or A_s), where ΔH is latent heat during martensitic or reverse martensitic transformation [i.e., the area under the endothermic/exothermic peaks in DSC curves as shown in Figs. 1(b1)–1(b6)]. M_s is the martensitic transformation start temperature and A_s is the reverse martensitic transformation start temperature. The martensitic transformation is generally considered as a first-order transformation, and its order parameter (spontaneous strain) will show a sudden jump at the transformation temperature during cooling and heating, and thus the latent heat of transformation will appear. Interestingly, as Pd content slightly increases from 0Pd to 7.5Pd, the entropy change drastically decreases to zero. Such a situation suggests that Pd atoms lower the thermodynamic stability of martensite and eventually result in a zero entropy change (i.e., nontransforming) region, being similar to the result in $Ti_{50-x}Ni_{50+x}$ alloys with strain glass state [7,40]. However, it is worth mentioning that Pd atoms in $Ti_{50}Ni_{50-x}Pd_x$ alloys do not lead to a nontransforming region but result in a phase boundary separating B19′ ($P21/m$, monoclinic structure [33]) and B19 ($Pmmb$, orthorhombic structure [33]) ferroelastic phases [32–34]. The reason will be discussed later. Notably, the entropy change dramatically reappears when Pd content exceeds 15Pd, indicating the martensitic phase becomes stable again over 15Pd. This intriguing result is rarely reported in the prior reported strain glass cases [26,27,40].

It is notable that the original ferroelastic phase and the revived ferroelastic phase belong to two different structures, as supported by electrical resistivity and XRD measurements in Fig. 2. In Figs. 2(a1) and 2(a2), a sharp resistivity change at M_s with an obvious hysteresis is observed at 0Pd and 3Pd during

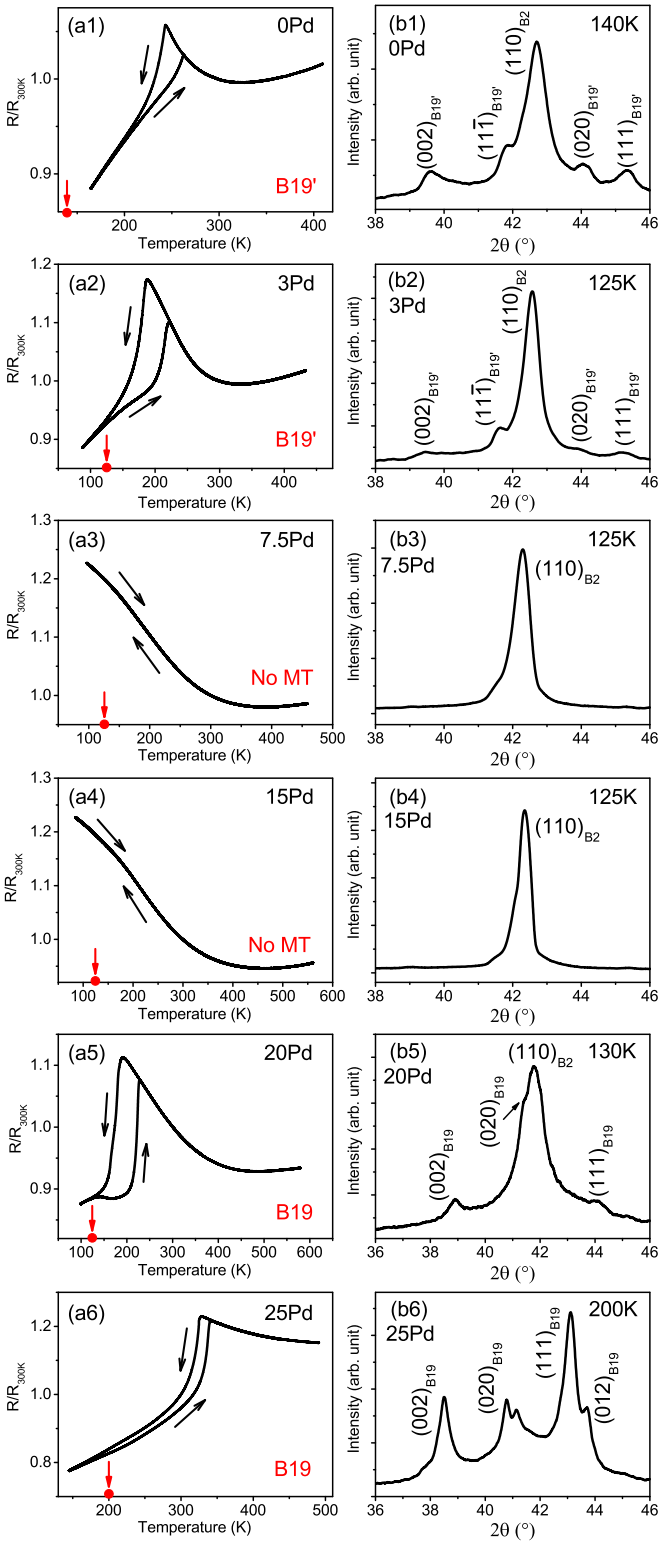

FIG. 2. (a1)–(a6) Electrical resistivity curves of (a1) 0Pd, (a2) 3Pd, (a3) 7.5Pd, (a4) 15Pd, (a5) 20Pd, and (a6) 25Pd. All the ER results are normalized by the electrical resistivity at 300 K. (b1)–(b6) X-ray diffraction patterns of typical (110) peaks in B2 structure of (b1) 0Pd, (b2) 3Pd, (b3) 7.5Pd, (b4) 15Pd, (b5) 20Pd, and (b6) 25Pd at temperature far below M_s, as indicated by red circles and arrows in the corresponding resistivity curves.

heating and cooling, respectively. The corresponding XRD profiles in Figs. 2(b1) and 2(b2) indicate that the ferroelastic structure is B19′ phase below M_s. (The XRD temperature is indicated by the red circles and arrows in the resistivity curves). When Pd concentration increases to the zero entropy change region (7.5Pd–15Pd), the resistivity curves in Figs. 2(a3) and 2(a4) respectively show an anomalous increase without any hysteresis during cooling and heating. Meanwhile, Figs. 2(b3) and 2(b4) show that the average structure still maintains B2 structure at a quite low temperature in this region. The negative temperature dependence (NTD) of electrical resistivity and the unchanged average structure in the nontransforming region are characteristics of a strain glass state, and similar behavior can also be found in Ni-rich Ti-Ni or Fe-doped Ti-Ni strain glass cases [28,40]. When Pd concentration further increases over 15Pd, a sudden resistivity change, however, recurs. As shown in Figs. 2(a5) and 2(a6), 20Pd and 25Pd exhibit obvious resistivity hysteresis loops again while the shape of 25Pd is quite different from that of 0Pd and 3Pd. Since electrical resistivity is sensitive to phase transformation, the shape difference of resistivity loops suggests the structure of the revived ferroelastic phase is different from that of the original one. In fact, the XRD profiles of 20Pd and 25Pd in Figs. 2(b5) and 2(b6) both show a B19 ferroelastic phase. Thus, with Pd concentration increasing, the system gradually changes from B19′ martensite (<7.5Pd) through a nontransforming region (7.5Pd–15Pd), and finally to revived B19 martensite (>15Pd).

In order to figure out what happens in the nontransforming region, anelastic property evolutions with temperature of different compositions (0Pd–25Pd) are investigated with DMA measurements. As shown in Fig. 3(a), 0Pd only displays one dip in the storage modulus curve with cooling, corresponding to a martensitic transformation from B2 to B19′ phase. 3Pd in Fig. 3(b), however, exhibits two anomalies upon cooling. The dip at higher temperature (∼213 K) exhibits frequency dependence (i.e., dip temperatures decrease with frequency lowering) revealing that a strain glass transition happens, while the other dip at lower temperature (∼193 K) suggests that a spontaneous transition from a frozen strain glass state to a long-range-ordered ferroelastic phase takes place [26]. The frequency dependence of the first dip follows the Vogel-Fulcher (V-F) relation [inset of Fig. 3(b)], yielding an ideal freezing temperature $T_0 \sim 204$ K. It is a feature of strain glass transition as previously reported [7,9,11,27,28]. With subsequent cooling, the appearance of the second dip and the corresponding sharp peak in the internal friction curves indicate that a long-range-ordered state forms. It is the B19′ ferroelastic phase as supported by the ER curve and XRD profile in Figs. 2(b1) and 2(b2). Thus, 3Pd undergoes a transition sequence from B2 phase to frozen strain glass to B19′ phase with cooling. By further increasing Pd concentration to 7.5Pd, there is only one dip accompanying modulus softening upon cooling, as shown in Fig. 3(c). The dip temperatures also exhibit frequency dispersion behavior, and T_0 is fitted as ∼176 K by the V-F fitting [inset of Fig. 3(c)]. It indicates there exists a strain glass transition in the nontransforming region. When Pd concentration reaches 15Pd, two anomalies in storage modulus curves accompanying modulus softening

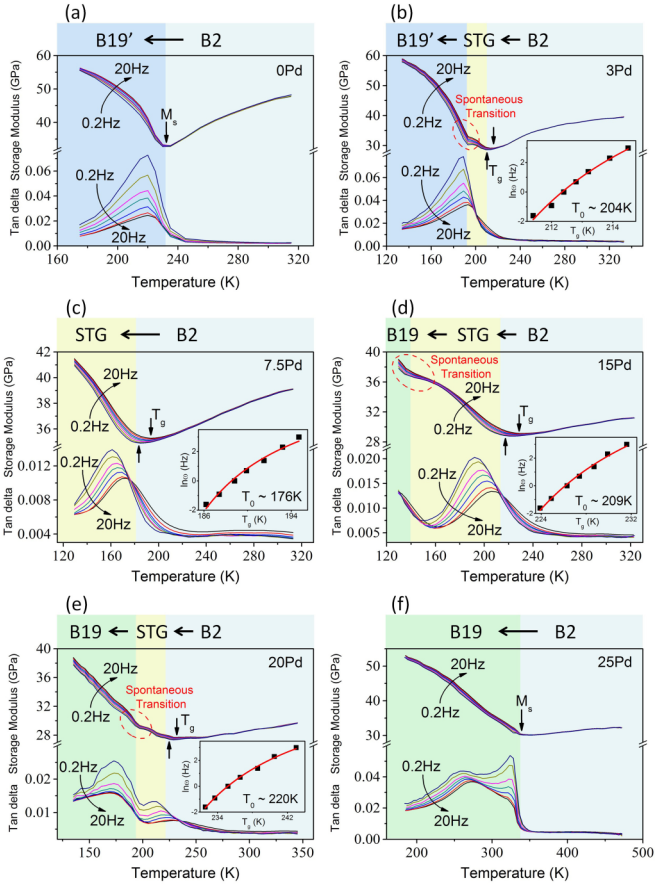

FIG. 3. Anelastic property evolutions with temperature for different Pd concentrations, (a) 0Pd, (b) 3Pd, (c) 7.5Pd, (d) 15Pd, (e) 20Pd, and (f) 25Pd. The inset figures exhibit V-F law fitting of each strain glass transition. The ideal freezing temperature (T_0) is yielded to be 204 K for 3Pd (b), 176 K for 7.5Pd (c), 209 K for 15Pd (d), and 220 K for 20Pd (e).

reappear with cooling in Fig. 3(d). Similarly to the result of 3Pd in Fig. 3(b), the first dip at higher temperature corresponds to a strain glass transition ($T_0 \sim 209$ K), while the second one at lower temperature is caused by a spontaneous transition. The difference lies at that with cooling the transition sequence of 15Pd is from B2 phase to frozen strain glass, and to B19 phase finally. 20Pd in Fig. 3(e) shares the same transition sequence as 15Pd, while the spontaneous transition temperature increases and the strain glass temperature range narrows. Such a strain glass temperature range finally disappears as Pd concentration further increases to 25Pd. Only one modulus dip corresponding to a B2-B19 martensitic transformation is detected at 25Pd in Fig. 3(f).

With all the above results, a sandwichlike strain glass phase diagram of $Ti_{49}Ni_{51-x}Pd_x$ ($x = 0 \sim 25$) is determined. For comparison, the well-known $Ti_{50}Ni_{50-x}Pd_x$, is also considered [32]. Thus, a 3D phase diagram of $Ti_{50-y}Ni_{50+y-x}Pd_x$ ($x = 0 \sim 25$, $y = 0 \sim 1$) is shown in Fig. 4. It is worth comparing the MPB phase diagram of $Ti_{50}Ni_{50-x}Pd_x$ with the sandwichlike phase diagram of $Ti_{49}Ni_{51-x}Pd_x$. The similarity is that the martensitic transformation temperature decreases in the B19′ region while it increases in the B19 region with Pd concentration increasing in both of the phase diagrams.

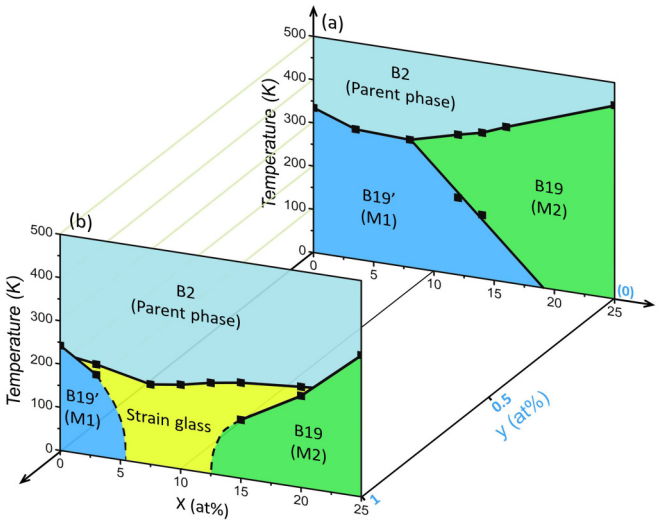

FIG. 4. 3D phase diagram of $Ti_{50-y}Ni_{50+y-x}Pd_x$ ($x = 0 \sim 25$, $y = 0 \sim 1$). (a) MPB phase diagram of $Ti_{50}Ni_{50-x}Pd_x$ ($x = 0 \sim 25$) (data comes from Ref. [32]). (b) Sandwichlike strain glass phase diagram of $Ti_{49}Ni_{51-x}Pd_x$ ($x = 0 \sim 25$).

This M_s change tendency suggests Pd doping lowers the thermodynamic stability of B19′ martensite while it stabilizes the B19 martensite. However, in the MPB phase diagram of $Ti_{50}Ni_{50-x}Pd_x$, Pd itself is unable to disturb the formation of the long-range-ordered B19′ ferroelastic phase. As the result, there is a phase boundary separating B19′ and B19 martensites. On the contrary, a slight deviation with 1 at. % Ni modification at ends, i.e., from $Ti_{50}Ni_{50}/Ti_{50}Pd_{50}$ to $Ti_{49}Ni_{51}/Ti_{49}Pd_{51}$, causes significant change: the phase boundary disappears, and instead, a strain glass region emerges, sandwiched between B19′ and B19 martensites. It is known that the excess of Ni reduces the stability of B19′ martensite as M_s decreases from $Ti_{50}Ni_{50}$ to $Ti_{49}Ni_{51}$ [40,41]. Thus, under assistance of 1 at. % excess Ni, Pd is able to drive the system to a glassy state.

IV. DISCUSSION

We then try to figure out the underlying mechanism on how this 3D phase diagram forms by providing a qualitative explanation. Previous work on standard strain glass phase diagrams reveals that the nontransforming end contributes two parts of effects: a global effect, which decreases the thermodynamic stability of long-range-ordered martensite, and a local effect to generate random local energy barriers which frustrate the system and lead to a glassy state [27]. On the other hand, the MPB phase diagram is always attributed to the competition between two ferroic phases from each side. But the local effect due to transforming doping is always beyond consideration [12,15]. It seems that previous understanding on both glass phase diagrams and MPB phase diagrams is too confined to explain this 3D phase diagram, especially the sandwichlike glass phase diagram part.

In fact, introducing a transforming end may generate three different effects: (1) one global effect to destabilize the ferroic matrix phase, (2) another global effect to stabilize another ferroic phase different from the matrix one, and (3) a local effect to create random local fields. In the following, a

phenomenological Landau-type model is proposed to understand the 3D phase diagram in Fig. 4.

In the case of MPB, two different ferroic orderings compete with each other. A generic Landau polynomial of the two ferroic phases that captures the essential features of the martensitic transitions of the two martensites can be expressed as [42,43]

$$F_A(x,T,\eta) = A_1\left(T - T_c^A\right)\eta^2 + A_2\eta^4 + A_3\eta^6, \quad (1)$$

$$F_B(x,T,\theta) = B_1\left(T - T_c^B\right)\theta^2 + B_2\theta^4 + B_3\theta^6, \quad (2)$$

where x is the concentration of doping end, T represents temperature, and η and θ are order parameters characteristic of the two martensitic phases. It should be noted that this is a simplified treatment. A more quantitative treatment requires the identification of the specific order parameters by symmetry analysis, and thus can be done with a more rigorous Landau polynomial based on those order parameters related to symmetries [44–47]. $A_1 \sim A_3$ and $B_1 \sim B_3$ are the expansion coefficients, related to the moduli of the system. Here they are treated as constants [42]. The effective transformation temperatures T_c^A and T_c^B are assumed to be linearly dependent on composition, $T_c^A = T_c^{A0} - \alpha x$ and $T_c^B = T_c^{B0} - \beta(1-x)$. Such a linear dependence is consistent with the tendency of the transformation temperature as a function of composition in Fig. 4. The α and β characterize the global effect strengths for different ferroic phases respectively [43]. The total free energy of the system is then written as [42]

$$\begin{aligned} F(x,T,\eta,\theta) = {} & A_1\left[T - \left(T_c^{A0} - \alpha x\right)\right]\eta^2 + A_2\eta^4 + A_3\eta^6 \\ & + B_1\left\{T - \left[T_c^{B0} - \beta(1-x)\right]\right\}\theta^2 \\ & + B_2\theta^4 + B_3\theta^6 + C\eta^2\theta^2, \end{aligned} \quad (3)$$

where $C\eta^2\theta^2$ describes the coupling between two order parameters. In the MPB phase diagram, the relative stability of these two ferroic phases varies with composition. At MPB, the free energies of the two phases are identical, that is, $F_A = F_B$. A Landau free energy landscape of the system at MPB is then schematically shown in Fig. 5(a).

In order to better understand the MPB phase diagram, we provide the free energy landscapes along different order parameter directions by Eq. (3) with suitable coefficients in Figs. 5(b1)–5(b3), which schematically shows the evolution of Landau free energy landscapes with composition at a certain temperature (below M_s) in the $Ti_{50}Ni_{50-x}Pd_x$ system. At the doping-free ($Ti_{50}Ni_{50}$, one end of the MPB phase diagram) case [Fig. 5(b1)], B19′ martensite is the only thermodynamic stable state below M_s (illustrated by two-energy valleys in the blue curve), while B19 martensite is unstable (illustrated by single-energy valley in the green curve). With doping Pd (i.e., increasing $Ti_{50}Pd_{50}$ concentration, the other end of the MPB phase diagram), the free energy of B19 martensite gradually declines, while the free energy of B19′ martensite starts to increase. The free energy of B19 martensite becomes comparable with that of B19′ martensite near the phase boundary, as shown in Fig. 5(b2). When Pd concentration further increases to the $Ti_{50}Pd_{50}$-rich side, the free energy of B19 martensite begins to be lower than that of B19′ martensite. Thus, B19 martensite, instead of B19′ martensite, turns thermodynamically stable,

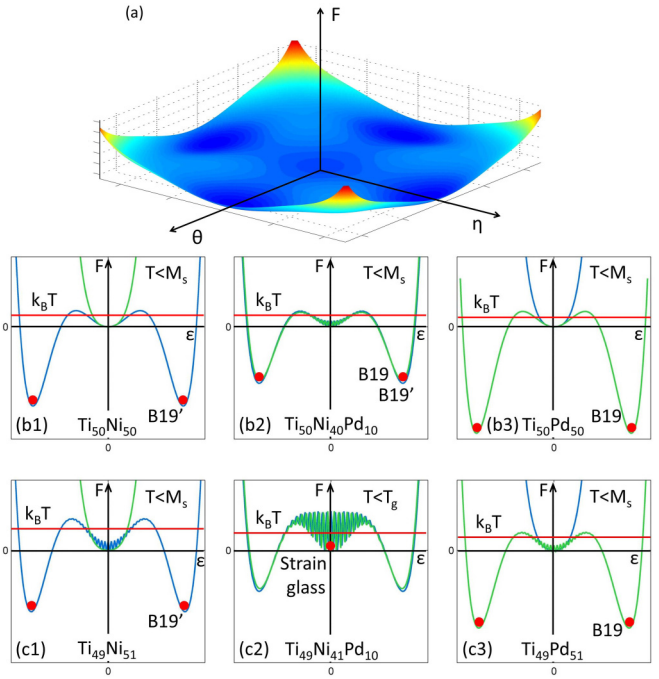

FIG. 5. Schematic Landau free energy landscapes used to explain how the 3D phase diagram of $Ti_{50-y}Ni_{50+y-x}Pd_x$ forms. (a) A prototype of 3D Landau free energy landscape. (b1)–(b3) describe the MPB phase diagram of $Ti_{50}Ni_{50-x}Pd_x$, corresponding to three typical compositions, (b1) $Ti_{50}Ni_{50}$, (b2) $Ti_{50}Ni_{40}Pd_{10}$, and (b3) $Ti_{50}Pd_{50}$. (c1)–(c3) describe the sandwichlike glass phase diagram of $Ti_{49}Ni_{51-x}Pd_x$ based on (c1) $Ti_{49}Ni_{51}$, (c2) $Ti_{49}Ni_{41}Pd_{10}$, and (c3) $Ti_{49}Pd_{51}$. ϵ represents the order parameters η and θ.

and becomes the only thermodynamic stable phase at the other end composition ($Ti_{50}Pd_{50}$) at last [see Fig. 5(b3)].

Doping Pd may also generate local energy barriers [denoted by zigzag lines near the ordinate origin in Fig. 5(b2)]. However, these local energy barriers are too small to hinder the formation of long-range-ordered martensites. Thus, previous models on MPB generally omitted the local effect, and only considered the competition between the two global effects.

In the case of the glass phase diagram, the nontransforming dopants decrease the global transition temperature while they create random local fields. The former is described by the composition (x) dependence of transition temperature (T_c), i.e., $T_c = T_c^0 - \alpha x$. The latter is considered as a spatially distributed random field $\sigma_{(\vec{r})}$ coupled to the order parameter. The free energy at location $\vec{r}$ is given by [43]

$$\begin{aligned} f_A(x,T,\eta_{(\vec{r})}) = {} & A_1\left[T - \left(T_c^{A0} - \alpha x\right)\right]\eta_{(\vec{r})}^2 + A_2\eta_{(\vec{r})}^4 \\ & + A_3\eta_{(\vec{r})}^6 - \sigma_{(\vec{r})}\eta_{(\vec{r})}. \end{aligned} \quad (4)$$

Thus the free energy of the whole system is

$$F_A(x,T,\eta) = \int dr[f_A(x,T,\eta_{(\vec{r})})]. \quad (5)$$

Such a model is suitable to describe the reported glass phase diagrams of $Ti_{50}Ni_{50-x}D_x$ and $Ti_{50}Pd_{50-x}D_x$ systems with the ferroic orderings of B19′ and B19, respectively [27,48]. D represents the nontransforming dopants, such as Mn, Cr, Fe,

V, etc., which create strong random local fields to the systems and give rise to the glassy state.

In the case of the sandwichlike phase diagram, all of the above three effects should be considered, but none of them is dominant. Consequently, all the effects contribute to the free energy, which is given by

$$F(x,T,\eta,\theta) = \int dr\big[f_A(x,T,\eta_{(\vec{r})}) + f_B(x,T,\theta_{(\vec{r})}) + C\eta^2_{(\vec{r})}\theta^2_{(\vec{r})}\big]. \quad (6)$$

In order to schematically draw the Landau free energy landscapes along two order parameter directions according to Eq. (6), we first consider the system as a homogeneous model like Eq. (3), and then add the local effect as random noise in the energy landscape, as used in the spin glass literature [4]. Thus, the local effect is denoted by zigzag lines near the ordinate origin in Fig. 5. Compared with $Ti_{50}Ni_{50}$, $Ti_{49}Ni_{51}$, the starting point of the sandwichlike glass phase diagram of $Ti_{49}Ni_{51-x}Pd_x$, has already possessed low intensity of local energy barriers caused by extra Ni atoms. Thus, local random fields in $Ti_{49}Ni_{51-x}Pd_x$ become stronger than those in $Ti_{50}Ni_{50-x}Pd_x$ at the same Pd concentration.

The sandwichlike strain glass phase diagram is then explained by Figs. 5(c1)–5(c3) which are obtained according to Eq. (6) with artificial coefficients. As shown in Fig. 5(c1), though the matrix becomes "dirty" compared with $Ti_{50}Ni_{50}$, this part of the local energy barriers in the matrix is not strong enough to interrupt the formation of B19′ martensite [40,41]. When the other end member ($Ti_{49}Pd_{51}$) is introduced, B19′ martensite further loses its thermodynamic stability while the stability of B19 martensite starts to increase. However, the most notable point in Fig. 5(c2) is that doping Pd atoms (i.e., $Ti_{49}Pd_{51}$) also generates random local energy barriers. This part of local energy barriers caused by Pd itself is still not enough to drive the system into a glass state [see Fig. 5(b2)], but with the assistance of local energy barriers existing in the matrix ($Ti_{49}Ni_{51}$), the total local energy barriers finally beat the thermodynamic driving force for long-range-ordered martensites (including both B19′ and B19 martensites), and result in a glassy state. Further increasing Pd concentration to the $Ti_{49}Pd_{51}$-rich side, the free energy valley of B19 martensite becomes even deeper, and the local energy barriers to interrupt the formation of B19 martensite become smaller because $Ti_{49}Pd_{51}$ prefers B19 martensite, as shown in Fig. 5(b3).

The competition among the three effects explains why the 3D phase diagram of $Ti_{50-y}Ni_{50+y-x}Pd_x$ forms. In the MPB phase diagram of $Ti_{50}Ni_{50-x}Pd_x$, the two competing global effects are dominant, while the local effect is negligible. In the sandwichlike phase diagram of $Ti_{49}Ni_{51-x}Pd_x$, the net global effect (from the competition of two global effects) and the local effect are comparable with each other, and the competition between them results in the sandwiched glass region. Thus, the transforming doping end is considered to be able to create a local effect (i.e., random local energy barriers). This is supported by our sandwichlike phase diagram. Last but not least, one may easily imagine the phase diagram with further modifying two ends to $Ti_{48}Ni_{52}$/$Ti_{48}Pd_{52}$: it should be a traditional strain glass phase diagram since the $Ti_{48}Ni_{52}$ end is nontransforming (strain glass) [40], while the $Ti_{48}Pd_{52}$ end is transforming [49]. Thus, the sandwichlike strain glass phase diagram of $Ti_{49}Ni_{51}$-$Ti_{49}Pd_{51}$ serves as a bridge linking the MPB phase diagram of $Ti_{50}Ni_{50}$-$Ti_{50}Pd_{50}$ and the strain glass phase diagram of $Ti_{48}Ni_{52}$-$Ti_{48}Pd_{52}$.

V. CONCLUSIONS

In conclusion, we reported a sandwichlike strain glass phase diagram in $Ti_{49}Ni_{51-x}Pd_x$ and established a 3D phase diagram of $Ti_{50-y}Ni_{50+y-x}Pd_x$. This sandwichlike glass phase diagram enables us to have a comprehensive understanding on how a transforming doping end influences a transforming matrix: (1) to destabilize the ferroic matrix phase, (2) to stabilize another ferroic phase different from the matrix one, and (3) to create random local fields. This understanding may guide us to unify prior models on respectively explaining the glass and MPB phase diagrams, and may bring about new physics on doping effects.

ACKNOWLEDGMENTS

The authors gratefully acknowledge the support of the National Basic Research Program of China (2012CB619401, 2014CB644003), National Natural Science Foundation of China (51431007, 51621063, 51320105014, 51571156, 51671156, 51671157, 51501145, 51601140), Program for Changjiang Scholars and Innovative Research Team in University (IRT13034), and Program of Introducing Talents of Discipline to Universities in China (B06025).

[1] R. W. Cahn, Nat. Mater. **1**, 3 (2002).
[2] S. M. Sze, *Physics of Semiconductor Devices* (John Wiley, New York, 1981).
[3] V. K. Wadhawan, *Introduction to Ferroic Materials* (Gordon and Breach, Amsterdam, 2000).
[4] J. A. Mydosh, *Spin Glasses* (Taylor and Francis, London, 1993).
[5] L. E. Cross, Ferroelectrics **76**, 241 (1987).
[6] D. Viehland, M. Wuttig, and L. Cross, Ferroelectrics **120**, 71 (1991).
[7] S. Sarkar, X. Ren, and K. Otsuka, Phys. Rev. Lett. **95**, 205702 (2005).
[8] Y. Nii, T. H. Arima, H. Y. Kim, and S. Miyazaki, Phys. Rev. B **82**, 214104 (2010).
[9] J. Y. Liu, M. J. Jin, C. Ni, Y. Shen, G. L. Fan, Z. Wang, Y. Zhang, C. F. Li, Z. Q. Liu, and X. J. Jin, Phys. Rev. B **84**, 140102 (2011).
[10] Y. Zhou, D. Xue, Y. Tian, X. Ding, S. Guo, K. Otsuka, J. Sun, and X. Ren, Phys. Rev. Lett. **112**, 025701 (2014).
[11] J. A. Monroe, J. E. Raymond, X. Xu, M. Nagasako, R. Kainuma, Y. I. Chumlyakov, R. Arroyave, and I. Karaman, Acta Mater. **101**, 107 (2015).
[12] B. Jaffe, W. R. Cook, and H. Jaffe, *Piezoelectric Ceramics* (Academic Press, London, 1971).
[13] G. H. Haertling, J. Am. Ceram. Soc. **82**, 797 (1999).
[14] M. Ahart, M. Somayazulu, R. E. Cohen, P. Ganesh, P. Dera, H.-k. Mao, R. J. Hemley, Y. Ren, P. Liermann, and Z. Wu, Nature (London) **451**, 545 (2008).

[15] W. Liu and X. Ren, Phys. Rev. Lett. **103**, 257602 (2009).
[16] S. Yang, H. Bao, C. Zhou, Y. Wang, X. Ren, Y. Matsushita, Y. Katsuya, M. Tanaka, K. Kobayashi, X. Song, and J. Gao, Phys. Rev. Lett. **104**, 197201 (2010).
[17] R. Bergstrom, Jr., M. Wuttig, J. Cullen, P. Zavalij, R. Briber, C. Dennis, V. O. Garlea, and M. Laver, Phys. Rev. Lett. **111**, 017203 (2013).
[18] X. Ren and K. Otsuka, Nature (London) **389**, 579 (1997).
[19] A. Saxena, Int. Ferroelectr. **131**, 3 (2011).
[20] T. Lookman, D. Xue, R. Vasseur, H. Zong, and X. Ding, Phys. Status Solidi B **251**, 2003 (2014).
[21] D. Xue, Y. Zhou, X. Ding, Y. Wang, J. Zhang, J. Sun, and X. Ren, Phys. Status Solidi B **251**, 2019 (2014).
[22] Y. Wang, X. Ren, K. Otsuka, and A. Saxena, Phys. Rev. B **76**, 132201 (2007).
[23] P. Lloveras, T. Castan, M. Porta, A. Planes, and A. Saxena, Phys. Rev. Lett. **100**, 165707 (2008).
[24] P. Lloveras, T. Castan, M. Porta, A. Planes, and A. Saxena, Phys. Rev. B **80**, 054107 (2009).
[25] R. Vasseur and T. Lookman, Phys. Rev. B **81**, 094107 (2010).
[26] R. Vasseur, D. Xue, Y. Zhou, W. Ettoumi, X. Ding, X. Ren, and T. Lookman, Phys. Rev. B **86**, 184103 (2012).
[27] Y. Zhou, D. Xue, X. Ding, Y. Wang, J. Zhang, Z. Zhang, D. Wang, K. Otsuka, J. Sun, and X. Ren, Acta Mater. **58**, 5433 (2010).
[28] D. Wang, Z. Zhang, J. Zhang, Y. Zhou, Y. Wang, X. Ding, Y. Wang, and X. Ren, Acta Mater. **58**, 6206 (2010).
[29] X. Dai, A. DiGiovanni, and D. Viehland, J. Appl. Phys. **74**, 3399 (1993).
[30] H. Liu, R. Harrison, and A. Putnis, J. Appl. Phys. **90**, 6321 (2001).
[31] B. R. Coles, B. V. B. Sarkissian, and R. H. Taylor, Philos. Mag. **37**, 489 (1978).
[32] K. Otsuka and C. M. Wayman, *Shape Memory Materials* (Cambridge University Press, Cambridge, 1998).
[33] K. Otsuka and X. Ren, Prog. Mater. Sci. **50**, 511 (2005).
[34] S. Miyazaki and A. Ishida, Mater. Sci. Eng. A **273–275**, 106 (1999).
[35] N. Matveeva, V. Khachin, and V. Sivokha, *Stable and Metastable Phase Equilibrium in Metallic Systems* (in Russian) (Nauka Publishers, Moscow, 1985).
[36] A. A. Klopotov, V. P. Sivokha, N. M. Matveeva, and Y. A. Sazanov, Russ. Phys. J. **36**, 526 (1993).
[37] V. Khachin, Revue Phys. Appliquee **24**, 733 (1989).
[38] A. Loidl, Annu. Rev. Phys. Chem. **40**, 29 (1989).
[39] N. Korner, Ch. Pfammatter, and R. Kind, Phys. Rev. Lett. **70**, 1283 (1993).
[40] Z. Zhang, Y. Wang, D. Wang, Y. Zhou, K. Otsuka, and X. Ren, Phys. Rev. B **81**, 224102 (2010).
[41] J. Frenzel, E. P. George, A. Dlouhy, C. Somsen, M. F. X. Wagner, and G. Eggeler, Acta Mater. **58**, 3444 (2010).
[42] E. K. H. Salje, *Phase Transitions in Ferroelastic and Co-Elastic Crystals* (Cambridge University Press, Cambridge, 1990).
[43] D. Wang, Y. Wang, Z. Zhang, and X. Ren, Phys. Rev. Lett. **105**, 205702 (2010).
[44] G. R. Barsch and J. A. Krumhansl, Phys. Rev. Lett. **53**, 1069 (1984).
[45] G. R. Barsch, Mater. Sci. Forum **327-328**, 367 (2000).
[46] T. Lookman, S. R. Shenoy, K. O. Rasmussen, A. Saxena, and A. R. Bishop, Phys. Rev. B **67**, 024114 (2003).
[47] A. Saxena and T. Lookman, in *Handbook of Materials Modeling*, edited by S. Yip (Springer, Berlin, 2005).
[48] Y. Zhou, D. Xue, X. Ding, K. Otsuka, J. Sun, and X. Ren, Phys. Status Solidi B **251**, 2027 (2014).
[49] H. Donkersloot and J. Van Vucht, J. Less-Common Met. **20**, 83 (1970).